

# Stochastic model for the hydrodynamic force in Euler–Lagrange simulations of particle-laden flows

Aaron M. Lattanzi <sup>1,\*</sup> Vahid Tavanashad <sup>2</sup>  
Shankar Subramaniam <sup>2</sup> and Jesse Capecelatro <sup>1,3</sup>

<sup>1</sup>*Department of Mechanical Engineering, University of Michigan, Ann Arbor, Michigan 48109, USA*

<sup>2</sup>*Department of Mechanical Engineering, Iowa State University, Ames, Iowa 50011, USA*

<sup>3</sup>*Department of Aerospace Engineering, University of Michigan, Ann Arbor Michigan 48109, USA*



(Received 22 March 2021; accepted 17 December 2021; published 3 January 2022)

Standard Eulerian–Lagrangian (EL) methods generally employ drag force models that only represent the mean hydrodynamic force acting upon a particle-laden suspension. Consequently, higher-order drag force statistics, arising from neighbor-induced flow perturbations, are not accounted for; this has implications on the predictions for particle velocity variance and dispersion. We develop a force Langevin model that treats neighbor-induced drag fluctuations as a stochastic force within an EL framework. The stochastic drag force follows an Ornstein-Uhlenbeck process and requires closure of the integral timescale for the fluctuating hydrodynamic force and the standard deviation in drag. The former is closed using the mean-free time between successive collisions, derived from the kinetic theory of nonuniform gases. For the latter, particle-resolved direct numerical simulation (PR-DNS) of fixed particle assemblies is utilized to develop a correlation. The stochastic EL framework specifies unresolved drag force statistics, leading to the correct evolution and sustainment of particle velocity variance over a wide range of Reynolds numbers and solids volume fractions, when compared to PR-DNS of freely evolving homogeneous suspensions. By contrast, standard EL infers drag statistics from variations in the resolved flow and thus underpredicts the growth and steady particle velocity variance in homogeneous suspensions. Velocity statistics from standard EL approaches are found to depend on the bandwidth of the projection function used for two-way momentum coupling, while results obtained from the stochastic EL approach are insensitive to the projection bandwidth.

DOI: [10.1103/PhysRevFluids.7.014301](https://doi.org/10.1103/PhysRevFluids.7.014301)

## I. INTRODUCTION

Eulerian–Lagrangian (EL) methods, in which particles are tracked individually and the fluid is solved on an Eulerian grid, have gained considerable traction for modeling particle-laden flows due to a balance between speed and resolution [1–4]. In recent years, emphasis has been placed on moderate to high mass loading where particles have a first-order effect on the underlying fluid flow disturbances, which feed back to the particle dynamics. Since EL methods do not resolve the fluid boundary layer at the surface of each particle, they enable grid spacings of the order of, or larger than, the particle diameter. The reduced resolution in EL methods requires a model for the hydrodynamic fluid-particle force. By contrast, particle-resolved direct numerical simulation (PR-DNS) resolves the fluid boundary layers around each particle, and thus, the interphase drag force is an output from such simulations. For strongly coupled flows with inertial particles, increasing the

---

\*alattanz@umich.edu

quantitative agreement between EL methods and PR-DNS requires critical assessment of the drag force model. Generally speaking, existing models for drag only capture low-order statistics, such as the mean hydrodynamic force exerted on a particle-laden suspension. It is now recognized that suspensions will exhibit significant variance in the drag force due to interactions between particles and fluid disturbances generated by their neighbors. Variance in drag force, arising from neighbor-induced fluid velocity fluctuations [pseudoturbulent kinetic energy (PTKE)] is generally ignored in EL frameworks. However, recent works have highlighted the importance of PTKE in particle-laden flows; see the closed-form model [5] and transport equations [6].

It has become increasingly well established that standard EL methods, which employ a mean drag closure and neglect PTKE-induced drag disturbances, underpredict drag variance when compared to PR-DNS [7–9]. To this end, multiple PR-DNS studies have demonstrated that flow past a collection of monodisperse spheres yields normally distributed drag forces [10–13] whose standard deviation is comparable in magnitude to its mean [10,12]. Due to the formation of fluid wakes (PTKE), particles will interact with each other indirectly over length scales comparable to their diameter. These particle-wake interactions give rise to short-range drag perturbations that drive relative motion between neighboring particles, such as drafting-kissing-tumbling (DKT) [14]. Therefore, neglecting higher-order drag statistics, resulting from neighbor effects, can detrimentally impact EL predictions for higher-order particle statistics (velocity variance and dispersion) [9]. To date, few drag models have been proposed that account for neighbor-induced disturbances, and which may be broadly grouped into deterministic [15–17] and stochastic [8,18,19] approaches. In the deterministic approach, the drag force experienced by a given particle is directly mapped to its pairwise neighbor interactions, requiring that the relative position of each particle be known when computing the drag force. It is worth noting that the aforementioned information is available in an EL framework but not in an Euler-Euler (EE) framework where the solids are treated as a continuum. By contrast, stochastic approaches aim to capture higher-order particle statistics, resulting from drag fluctuations, without detailed knowledge of each particle position.

Here, a statistical approach is employed to account for neighbor-induced drag fluctuations. Specifically, we follow the mathematical theory derived by Lattanzi *et al.* [19] for a hierarchy of Langevin equations and employ a stochastic drag force treatment. The interested reader is referred to the cited work for a more inclusive discussion on what the force Langevin (FL) framework yields in terms of particle-phase moments. However, we note that the fluctuating drag statistics obtained from an Ornstein-Uhlenbeck (OU) process were shown to be consistent with drag statistics extracted from freely evolving PR-DNS of homogeneous systems. Namely, the fluctuating drag is normally distributed with an exponentially decaying Lagrangian autocorrelation function. As a result of capturing the drag fluctuation statistics, the steady particle velocity variance obtained with FL also agreed with PR-DNS of homogeneously distributed inertial particles at moderate Reynolds numbers. In this manner, the stochastic drag force is designed to reproduce statistics obtained from fully resolved simulations and is not an empirically added fluctuation.

We emphasize that the present study is centered around a stochastic description of neighbor-induced drag disturbances, where the physical mechanism for drag perturbations is attributed to fluid flow disturbances generated by particles that are in close proximity. It should be noted that the concept of drag force disturbances is not specific to dense suspensions, but will also be present in under-resolved simulations of intrinsically turbulent flows, i.e., flows that are turbulent even in the absence of the disperse phase. Specifically, unresolved fluid velocity fluctuations also provide a source for particle drag disturbances in dilute flows where neighbor-induced effects are less significant. Pioneering works on turbulent single-phase flows [20–23] have developed Langevin equations for reconstructing the total fluid velocity that may be applied to dilute multiphase flows [24–26]. More recently, Gorokhovski and Zamansky [27] proposed a stochastic acceleration model for the drag force on particles smaller and larger than the Kolmogorov length scale. Similar to the approach taken here, Gorokhovski and Zamansky [27] decompose the particle drag force into a resolved and fluctuating contribution. Due to the emphasis on intrinsic turbulence, the fluctuating contribution in that work is parametrized through the instantaneous fluid dissipation rate seen by the

particle (modeled with a log-normal distribution [28]). Therefore, the Langevin models noted above for velocity and acceleration (fluid or particle) are akin to the force Langevin framework developed here, with a crucial difference being that closures for the stochastic process are appropriate for dilute turbulent flows without significant two-way coupling. Drag fluctuations arise in the former case from under-resolving the intrinsic fluid turbulence, while in the latter case, they arise from under-resolving the pseudoturbulence generated by boundary layers around neighboring particles.

The remainder of the paper is arranged as follows. In Sec. II, a statistical description is introduced for the hydrodynamic force felt by a particle in a dynamical suspension. The drag force is decomposed into a mean and fluctuating component, where the fluctuating component is a stochastic variable that specifies higher-order statistics. In Sec. III, closure is proposed for the fluctuating drag within homogeneous suspensions of inertial particles at moderate Reynolds numbers. Details regarding the numerics are provided in Sec. IV. Homogeneous fluidization of elastic particles is considered in Sec. V as a canonical flow for comparison to the PR-DNS data of Tenneti *et al.* [8] and Tavanashad *et al.* [29]. Specifically, depending upon the initial conditions, particle velocity variance in homogeneous fluidization will grow (heat) or decay (cool) to a steady state where neighbor-induced drag disturbances are balanced by hydrodynamic dissipation. Therefore, the ability of an EL method to capture the evolution of particle velocity variance in homogeneous fluidization is a significant test of the method's ability to capture higher-order drag statistics. We first demonstrate that the stochastic EL framework presented here yields convergent velocity variance in homogeneous fluidization, while the velocity variance resulting from standard EL inherently depends upon the length scale employed during two-way coupling (i.e., grid spacing or filter size). Next, the proposed stochastic EL framework is directly compared to PR-DNS data in the fluidized homogeneous heating system (FHHS) and fluidized homogeneous cooling system (FHCS). Finally, we assess the role of neighbor-induced drag fluctuations in a large-scale simulation of cluster-induced turbulence (CIT) in Sec. VI.

## II. A STATISTICAL DESCRIPTION OF DRAG

Particle motion follows Newton's second law where acceleration results from the net force acting upon the body. When considering the hydrodynamic drag force exerted on particle  $i$ ,  $\mathbf{F}_{\text{inter}}^{(i)}$ , an exact integration of the fluid stress tensor  $\check{\boldsymbol{\tau}}$  over the surface of a particle  $\Gamma$  may be evaluated as

$$\mathbf{F}_{\text{inter}}^{(i)} = \int_{\Gamma} \check{\boldsymbol{\tau}} \cdot \mathbf{n} dA, \quad (1)$$

where  $\check{(\cdot)}$  denotes a microscale quantity prior to any averaging,  $dA$  is an infinitesimal area element, and  $\mathbf{n}$  is the unit normal vector outward from the particle surface. For an *isolated* sphere subject to nonuniform Stokes flow, Maxey and Riley [30] consider a rigorous evaluation of Eq. (1) that yields contributions from the undisturbed fluid flow, quasisteady drag, added mass, and Basset history:  $\mathbf{F}_{\text{inter}}^{(i)} = \mathbf{F}_{\text{un}}^{(i)} + \mathbf{F}_{\text{qs}}^{(i)} + \mathbf{F}_{\text{am}}^{(i)} + \mathbf{F}_{\text{uv}}^{(i)}$ . However, for a general dynamic suspension, finite Reynolds number effects and neighbor disturbances do not allow a first-principles solution to be obtained. Consequently, standard EL methods generally rely upon drag correlations.

Following Anderson and Jackson [31], the fluid stress tensor in Eq. (1) may be decomposed into a filtered component  $\boldsymbol{\tau}$  and residual  $\boldsymbol{\tau}'$ , such that  $\check{\boldsymbol{\tau}} = \boldsymbol{\tau} + \boldsymbol{\tau}'$ . Employing the divergence theorem and choosing a filter length scale such that  $\boldsymbol{\tau}$  varies little over the volume of the particle, one obtains

$$\int_{\Gamma} \check{\boldsymbol{\tau}} \cdot \mathbf{n} dA = \mathcal{V}_p^{(i)} \nabla \cdot \boldsymbol{\tau}[\mathbf{X}_p^{(i)}] + \int_{\Gamma} \boldsymbol{\tau}' \cdot \mathbf{n} dA, \quad (2)$$

where  $\mathcal{V}_p^{(i)}$  is the volume of the particle and  $\boldsymbol{\tau}[\mathbf{X}_p^{(i)}]$  is the filtered stress tensor evaluated at the position of the particle  $\mathbf{X}_p^{(i)}$ . Traditionally, the unresolved drag force  $\int \boldsymbol{\tau}' \cdot \mathbf{n} dA$  is closed with correlations obtained from experiments [32–34] or PR-DNS [35–38]. However, these correlations only capture the average hydrodynamic force acting on a suspension. Consequently, particles that

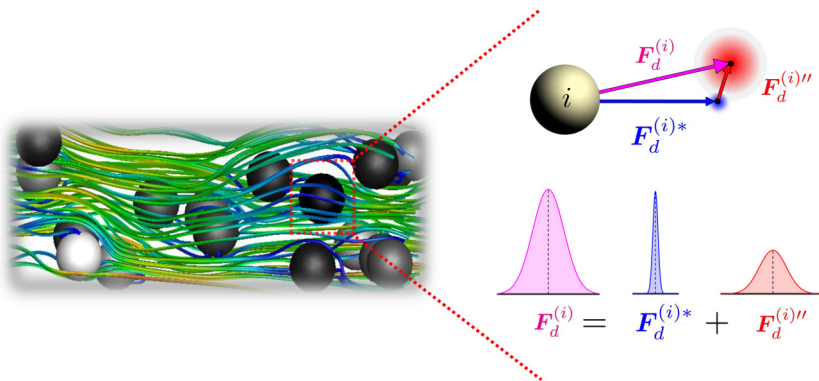


FIG. 1. Neighboring particles disturb the local flow field within a particle-laden suspension, leading to higher-order drag statistics. Negative fluid velocity fluctuations (blue streamlines) correspond to reduced drag forces (darker particles), while positive fluid velocity fluctuations (red streamlines) correspond to higher drag forces (lighter particles). A statistical description is adopted for the drag on an individual particle according to Eq. (3), where  $\mathbf{F}_d^{(i)''}$  allows specification of higher-order statistics.

experience the same filtered hydrodynamic environment will experience the same modeled drag force, even though the neighbor-induced flow may cause significant departure from the mean contribution to drag. Furthermore, traditional drag correlations lead to solely dissipative behavior for the particle velocity variance when applied to the PR-DNS data of freely evolving homogeneous suspensions, which is qualitatively incorrect [39]. It should be noted that the first term on the right-hand side of Eq. (2) takes the same form as  $\mathbf{F}_{\text{un}}^{(i)}$  in the classical formulation of Maxey and Riley [30], but inherently contains the effects of particle disturbances due to two-way coupling. The second term involving  $\boldsymbol{\tau}'$  contains all of the other contributions (quasisteady drag, added mass, and Basset history). Rather than attempting to tease out how each pairwise neighbor interaction contributes to the hydrodynamic forces on a given particle, we seek a statistical representation that treats these effects stochastically. To build upon the standard EL approach and account for neighbor effects, we expand the unresolved drag into a quasisteady contribution  $\mathbf{F}_d^{(i)*}$  and fluctuating  $\mathbf{F}_d^{(i)''}$  component according to

$$\int_{\Gamma} \boldsymbol{\tau}' \cdot \mathbf{n} dA = \mathbf{F}_d^{(i)*} + \mathbf{F}_d^{(i)''}, \quad (3)$$

where the double-prime notation is used here to denote a fluctuation around a modeled term, while the single-prime notation denotes a fluctuation with respect to a filtered quantity. Generally speaking,  $\mathbf{F}_d^{(i)''}$  corresponds to a perturbation from the quasisteady drag force. Here, we attribute force perturbations to fluid flow disturbances created by neighboring particles. Therefore,  $\mathbf{F}_d^{(i)''}$  is a stochastic variable whose statistics, such as distribution and time correlation, are designed to be consistent with PR-DNS of freely evolving particles. In this manner,  $\mathbf{F}_d^{(i)''}$  allows higher-order drag statistics, originating from neighbor effects, to be directly enforced within a fluidized suspension (see Fig. 1). Closure of the stochastic process utilized to model  $\mathbf{F}_d^{(i)''}$  is provided in Sec. III.

When applying the decomposition in Eq. (3) to an EL method, it must be noted that there are differences in how PR-DNS studies and EL methods characterize a system. Specifically, EL methods generally employ instantaneous particle velocities and locally interpolated fluid quantities when evaluating drag force correlations, whereas PR-DNS correlations are derived from ensemble-averaged quantities. To this end, we immediately define the mean Reynolds number employed by PR-DNS,

$$\text{Re}_m = (1 - \langle \phi \rangle) \frac{\rho_f d_p \|\langle \mathbf{W} \rangle\|}{\mu_f}, \quad (4)$$

and the particle Reynolds number employed by EL,

$$\text{Re}_p = (1 - \phi) \frac{\rho_f d_p \|\mathbf{u}_f[\mathbf{X}_p^{(i)}] - \mathbf{U}_p^{(i)}\|}{\mu_f}, \quad (5)$$

where  $\phi$  is the solids volume fraction,  $\rho_f$  is the fluid density,  $d_p$  is the particle diameter,  $\mu_f$  is the dynamic viscosity,  $\langle \mathbf{W} \rangle = \langle \mathbf{u}_f \rangle - \langle \mathbf{U}_p \rangle$  is the mean slip velocity, and  $\mathbf{u}_f$  and  $\mathbf{U}_p$  are the fluid and particle velocity, respectively. The  $\langle \cdot \rangle$  notation denotes an ensemble average, while the  $[\mathbf{X}_p^{(i)}]$  notation is suppressed on the solids volume fraction for readability. Therefore, the  $\mathbf{F}_d^{(i)*}$  contribution in EL, computed with the particle Reynolds number, will be an approximation to the ensemble-averaged mean drag force exerted on a suspension  $\langle \mathbf{F}_d \rangle$ . More precisely,  $\mathbf{F}_d^{(i)*}$  is a stochastic model for the mean hydrodynamic force, arising from one-particle statistics (position and velocity) in a filtered realization of the fluid field, that is based on a form of average drag from PR-DNS. Therefore,  $\mathbf{F}_d^{(i)*}$  is inherently coupled to the momentum filtering employed by EL and will approach a  $\delta$  function centered at  $\langle \mathbf{F}_d \rangle$  in the limit of infinite filter width; but for finite filter length scales,  $\mathbf{F}_d^{(i)*}$  will have finite variance due to variation of interpolated quantities and particle velocity (see Sec. V A). In the present work, the focus is given to filter widths larger than a particle diameter,  $\delta_f = O(10d_p)$ , that do not contribute to significant variation of  $\mathbf{F}_d^{(i)*}$  in homogeneous fluidization. To avoid confusion when discussing mean drag, we draw an analogy with the Maxey-Riley equation and refer to  $\mathbf{F}_d^{(i)*}$  as the quasisteady drag force. We further motivate this analogy by noting that the present work focuses on inertial particle suspensions where added mass and Basset history effects are less significant and PR-DNS correlations are obtained from fixed particle simulations.

### III. FORCE LANGEVIN FRAMEWORK

The force Langevin (FL) theory examined by Lattanzi *et al.* [19] is employed here to describe the neighbor-induced fluctuating drag force  $\mathbf{F}_d^{(i)''}$ . Specifically,  $\mathbf{F}_d^{(i)''}$  follows an Ornstein-Uhlenbeck (OU) process according to

$$d\mathbf{F}_d^{(i)''} = -\frac{1}{\tau_F} \mathbf{F}_d^{(i)''} dt + \sqrt{\frac{2}{\tau_F}} \sigma_F d\mathbf{W}_t, \quad (6)$$

where  $\tau_F$  is the integral timescale of the fluctuating drag force,  $\sigma_F$  is the standard deviation of the fluctuating drag force, and  $d\mathbf{W}_t$  is a Wiener process increment. We refer the interested reader to Lattanzi *et al.* [19], where a detailed discussion regarding motivation for, and results from, the OU process is provided. Here, we briefly emphasize that the steady solution to the OU process is a normal distribution  $\mathcal{N}[0, \sigma_F]$  and a multitude of PR-DNS studies have reported normally distributed drag forces  $\mathcal{N}[\langle F_d \rangle, \sigma_F]$  [7,10,12,13,18]. Additionally, FL was shown to be reconcilable with PR-DNS results for granular temperature evolution since it correctly attributes the source of granular temperature to the force-velocity covariance [19].

In general, coefficients of the OU process in Eq. (6), namely, the drag timescale  $\tau_F$  and standard deviation  $\sigma_F$ , may be tensorial quantities that correlate the drag fluctuations in each direction and drive anisotropic granular temperature development. While a valuable and interesting problem, we first consider the isotropic case given by Eq. (6) so that the same force timescale and standard deviation are applied to the fluctuating force in all three directions. We further note that particle collisions will relax the granular temperature back towards isotropy. For statistically homogeneous suspensions, Garzó *et al.* [40] derived an evolution equation for the particle velocity anisotropy tensor that shows a return to isotropy occurs at the steady state due to particle collisions. For dilute particle flows with small density ratio  $\rho_p/\rho_f = O(1)$ , where viscous lubrication is significant and particle collisions are less frequent, anisotropy may play a significant role. However, a description for such flows will need to be addressed in future work as the focus here is on inertial gas-solid suspensions.

### A. Force timescale

In principle, the fluctuating force timescale  $\tau_{F,ij}$  characterizes the memory of temporal correlation of the drag force fluctuation  $\mathbf{F}_d''$  and may be extracted from PR-DNS simulation with freely evolving particles via the Lagrangian covariance function,

$$\tau_{F,ij} = \int_0^\infty \frac{\langle F_{d,i}''(t+s)F_{d,j}''(t) \rangle}{\langle F_{d,i}''(t)F_{d,j}''(t) \rangle} ds, \quad (7)$$

where we note there is no sum over repeated force indices within the bracketed terms. The analysis by Lattanzi *et al.* [19] shows that FL generates a fluid-mediated source to particle velocity fluctuations through the force-velocity covariance. Specifically, the fluctuating drag forces drive the development of particle velocity fluctuations, and the time over which the fluctuating drag and particle velocity become correlated will dictate the magnitude of the granular temperature that can be developed.

In a dynamic suspension, particles will experience states of free streaming and redirection due to collisions. During free streaming, particles accelerate in the direction of the fluctuating drag force, developing force-velocity correlation [19]. However, interparticle collisions will act to redirect the particle velocity vector and decorrelate the fluctuating force and velocity. In the context of inertial particles, the mean-free time between collisions,  $\tau_{\text{col}}$ , is expected to provide an upper bound for the memory of the fluctuating force. Additionally,  $\tau_F \approx \tau_{\text{col}}$  was demonstrated in Table I of Lattanzi *et al.* [19] for inertial particles at moderate Reynolds numbers. It is also noteworthy that the Euler-Euler model developed by Koch and Sangani [41] for high Stokes number particles also considers the mean-free time as an approximation for  $\tau_F$ ; based upon arguments that the force integral timescale should be proportional to the timescale associated with rearrangement of the particle structure, which scales as  $d_p/\sqrt{\Theta}$ . However, oscillatory fluid wakes generated at high Reynolds numbers will act to reduce the force memory,  $\tau_F < \tau_{\text{col}}$ , and viscous lubrication in low density ratio flows will prevent collisions. For such cases, critical assessment of the closure for  $\tau_F$  will be needed. For the inertial particles and moderate Reynolds numbers considered here, we approximate the timescale for the fluctuating hydrodynamic force with the mean-free time between successive collisions (see Chap. 5 of [42]),

$$\tau_F \approx \tau_{\text{col}} = \frac{d_p}{24\phi\chi} \sqrt{\frac{\pi}{\Theta}}, \quad (8)$$

where  $\Theta$  is the granular temperature and  $\chi$  is the radial distribution function at contact for equilibrium systems [43],

$$\chi = \frac{1 + 2.50\phi + 4.51\phi^2 + 4.52\phi^3}{[1 - (\phi/0.64)^3]^{0.68}}. \quad (9)$$

At this point, two things should be noted. First,  $\tau_{\text{col}}$  is derived from the kinetic theory of nonuniform gases and thus is agnostic to PR-DNS data. Second, the granular temperature  $\Theta$  corresponds to spatially *uncorrelated* velocity fluctuations, while the particle velocity variance  $T$  does not employ spatial conditioning [44]. These two quantities are equivalent for homogeneous systems, where the spatially correlated mean equals the domain average, but not in inhomogeneous systems. We distinguish the granular temperature and particle velocity variance in nomenclature and mathematical computation; see Secs. IV D and V for more details regarding  $\Theta$  and  $T$ , respectively.

To further motivate  $\tau_F \approx \tau_{\text{col}}$  in the flows considered here, we apply the timescale analysis of Wylie *et al.* [45] and Mehrabadi *et al.* [5]. More specifically, Wylie *et al.* [45] proposed the ratio of hydrodynamic timescale,  $t_{\text{hydro}}$ , to mean collisional timescale,  $t_{\text{col}}$ , as a measure for the importance of hydrodynamic and collisional effects. For  $t_{\text{hydro}}/t_{\text{col}} \gg 1$ , Wylie *et al.* [45] assert that the flow is collisionally dominated. Following Mehrabadi *et al.* [5], we define  $t_{\text{hydro}} = \sqrt{3T}/\sigma_A$  and  $t_{\text{col}} = \bar{t}/\bar{N}_{\text{col}}$ , where  $\sigma_A$  is the standard deviation in hydrodynamic acceleration,  $\bar{N}_{\text{col}}$  is the average number

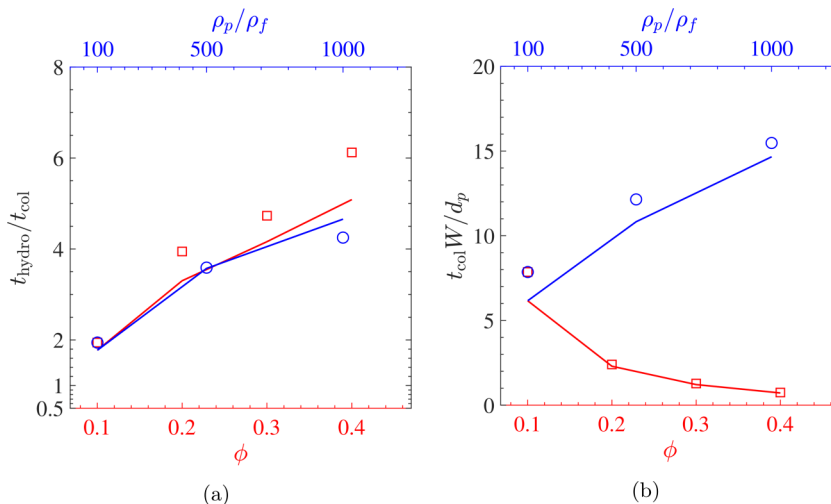


FIG. 2. (a)  $t_{\text{hydro}}/t_{\text{col}}$  as predicted by PR-DNS (markers) and theory (lines). (b)  $t_{\text{col}}$  as predicted by PR-DNS (markers) and theory (lines).

of collisions, and  $\bar{t}$  is the sample time over which collisions are counted. To quantify  $t_{\text{hydro}}/t_{\text{col}}$  in PR-DNS, we employ the velocity variance and acceleration standard deviation at the steady state and directly count collisions at the steady state. To draw comparison with theory, we employ the solution of Lattanzi *et al.* [46] to compute the hydrodynamic timescale at the steady state,

$$t_{\text{hydro}} = \sqrt{\frac{\tau_d^2 \tau_{\text{col}}(T_\infty)}{\tau_d + \tau_{\text{col}}(T_\infty)}}, \quad (10)$$

where  $1/\tau_d = F(\phi, \text{Re}_m)(1 - \phi)/\tau_p$  is the hydrodynamic timescale resulting from the quasisteady drag correlation; see Eq. (16). Additionally, the theory employs Eq. (8) to compute  $t_{\text{col}}$ . Since the timescales obtained from theory are a function of the steady particle velocity variance, we utilize  $T_\infty$  obtained from PR-DNS when computing the theoretical  $t_{\text{hydro}}$  and  $t_{\text{col}}$ . For  $\text{Re}_m = 20$ ,  $\phi \in [0.1, 0.4]$ , and  $\rho_p/\rho_f \in [100, 1000]$ , satisfactory agreement between theory and PR-DNS is obtained (see Fig. 2). Since the theory captures the collisional timescale, the hydrodynamic timescale must be reasonably approximated by the present formulation. It is noted that  $t_{\text{hydro}}/t_{\text{col}}$  in Fig. 2(a) is moderately underpredicted for  $\phi \geq 0.2$ , which implies  $\tau_F > \tau_{\text{col}}$ . For the conditions considered here,  $t_{\text{hydro}}/t_{\text{col}} \geq 2$  suggests collisional dominance. Furthermore, the flow becomes increasingly dominated by collisions at higher density ratios [larger Stokes numbers;  $\text{St} = \rho_p \text{Re}_m / (18\rho_f)$ ] and higher solids volume fractions, which are the expected trends. We now note that the results presented here differ markedly from those reported by Mehrabadi *et al.* [5], where  $t_{\text{hydro}}/t_{\text{col}} \ll 1$  was reported for similar conditions. The difference between the results presented here and those of Mehrabadi *et al.* [5] are due to corrected issues in the collision counting routine employed by Mehrabadi *et al.* [5]. Namely, the postprocessing script of Mehrabadi *et al.* [5] misses collision events, leading to artificially large  $t_{\text{col}}$ .

## B. Force standard deviation

In this section, the standard deviation in drag force is evaluated from PR-DNS of homogeneous fluid-particle suspensions. It has already been well established that the mean drag force exerted on a suspension of high inertia particles [ $\rho_p/\rho_f \geq O(100)$ ] is well approximated by PR-DNS simulation of static particle assemblies [35–37]. Moreover, Tavanashad *et al.* [47] recently performed PR-

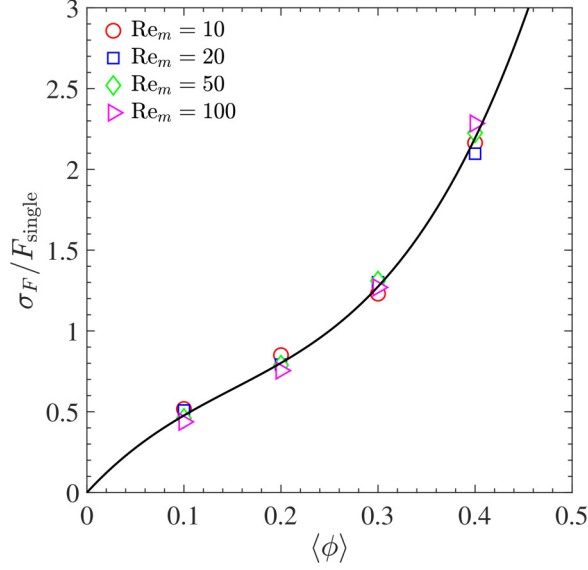


FIG. 3. Collapse of the drag force standard deviation  $\sigma_F$  obtained from PR-DNS when normalized by the drag force on an isolated sphere  $F_{\text{single}}$ . The black line corresponds to the correlation given by Eq. (12).

DNS with fixed and freely evolving particles over a wide range of conditions, including density ratio and Reynolds number, to study the effect of particle mobility on drag. It was shown that the corresponding drag correlation converges to the fixed bed correlation of Tenneti *et al.* [37] for large density ratios. In a similar fashion, a correlation for the standard deviation in drag force from the PR-DNS dataset of Tavanashad *et al.* [47] is pursued here. As was seen with mean drag, we observe convergence of the standard deviation in drag force  $\sigma_F$ , extracted from PR-DNS with freely evolving and fixed particle suspensions, at large particle-to-fluid density ratios  $\rho_p/\rho_f \geq 100$ . For this reason, a correlation is obtained from simulations with *fixed* particle assemblies. In the dataset of Tavanashad *et al.* [47], a simulation is defined by the mean solids volume fraction and mean Reynolds number. For a given set of conditions  $(\text{Re}_m, \langle \phi \rangle)$ , five particle configurations were generated, each containing 200 particles. In each realization, the mean drag force and standard deviation in drag force were computed in the direction of the mean slip velocity. Finally, the force standard deviation was ensemble averaged over all realizations.

When developing a mean drag force correlation for inertial particles, Tenneti *et al.* [37] showed that a solids volume fraction correction could be obtained for the normalized drag force  $\langle \mathbf{F}_d \rangle / F_{\text{single}}$ , where

$$F_{\text{single}} = 3\pi\mu_f d_p (1 + 0.15\text{Re}_m^{0.687})(1 - \langle \phi \rangle) \|\mathbf{W}\| \quad (11)$$

is the drag force on an isolated sphere given by the classic Schiller and Naumann correlation [48] and evaluated using the mean slip velocity. In a similar fashion, collapse of the normalized standard deviation  $\sigma_F / F_{\text{single}}$  is observed here, albeit onto a different function of solids volume fraction  $f_\phi^{\sigma_F}$  (see Fig. 3). A third-order polynomial in solids volume fraction is fit to the data to obtain

$$f_\phi^{\sigma_F} = 6.52\phi - 22.56\phi^2 + 49.90\phi^3, \quad (12)$$

which ensures that  $\lim_{\phi \rightarrow 0} \sigma_F = 0$ , i.e., there will be no neighbor-induced drag perturbations in the infinitely dilute limit. Thus, the standard deviation in drag may be readily modeled

in EL as

$$\frac{\sigma_F}{m_p^{(i)}} \equiv f_\phi^{\sigma_F} \frac{F_{\text{single}}}{m_p^{(i)}} = f_\phi^{\sigma_F} f_{\text{iso}} \frac{(1 - \phi) \|\mathbf{u}_f[\mathbf{X}_p^{(i)}] - \mathbf{U}_p^{(i)}\|}{\tau_p}, \quad (13a)$$

$$f_{\text{iso}} = (1 + 0.15\text{Re}_p^{0.687}), \quad (13b)$$

where  $m_p^{(i)} = \rho_p \mathcal{V}_p^{(i)}$  is the particle mass and  $\tau_p = \rho_p d_p^2 / (18\mu_f)$  is the Stokes response time.

Examination of Eqs. (12) and (13a) shows that the force standard deviation is written in terms of locally filtered fields and instantaneous particle velocities,  $\phi$ ;  $\text{Re}_p$ , so as to make it applicable to EL. Specifically, the correlation is developed from PR-DNS data with ensemble-averaged quantities  $\langle \cdot \rangle$ , but is intended for use in EL (see discussion at the end of Sec. II). In the absence of a more formal route for extending PR-DNS-derived correlations to EL methods, we proceed in the standard manner by replacing ensemble-averaged quantities with their locally filtered counterpart. Furthermore, it is reiterated that Eq. (13a) is for the standard deviation in drag (hydrodynamic force along the mean flow direction) and that the isotropic formulation in Eq. (6) will impose the same  $\sigma_F$  in all three directions. As noted in Sec. III, force anisotropy, which drives anisotropy in the particle velocity variance, may be included in the general framework; however, new correlations will need to be developed for such quantities.

#### IV. EULER-LAGRANGE FRAMEWORK

In this section, the stochastic EL framework and its discretization are summarized, using closures reported in Sec. III to model the drag force perturbations.

##### A. Particle-phase description

The translational motion of each particle follows Newton's second law according to

$$\frac{d\mathbf{X}_p^{(i)}}{dt} = \mathbf{U}_p^{(i)}, \quad (14a)$$

$$m_p^{(i)} \frac{d\mathbf{U}_p^{(i)}}{dt} = \sum_{j=1}^N \mathbf{F}_{\text{col}}^{(ij)} + \mathbf{F}_{\text{inter}}^{(i)} + m_p^{(i)} \mathbf{g}. \quad (14b)$$

A soft-sphere approach is employed for the collisional force  $\mathbf{F}_{\text{col}}$ , where each particle contact is described as a linear-spring-dashpot [1]. The simulation time step  $\Delta t$  is restricted such that particles do not move more than one-tenth of their diameter per time step, thereby avoiding excessive overlap [4]. A second-order Runge-Kutta (RK) scheme is utilized to integrate Eqs. (14a) and (14b) in time. Combining Eqs. (1)–(3), the interphase momentum exchange term  $\mathbf{F}_{\text{inter}}^{(i)}$  contains contributions from the resolved stress, quasisteady drag, and fluctuating drag according to

$$\mathbf{F}_{\text{inter}}^{(i)} = \mathcal{V}_p^{(i)} \nabla \cdot \boldsymbol{\tau}[\mathbf{X}_p^{(i)}] + \mathbf{F}_d^{(i)*} + \mathbf{F}_d^{(i)''}. \quad (15)$$

Since we are focusing on inertial particle suspensions, the quasisteady drag closure provided in Tenneti *et al.* [37] is employed here,

$$\frac{\mathbf{F}_d^{(i)*}}{m_p^{(i)}} = \left( \frac{f_{\text{iso}}}{(1 - \phi)^2} + f_\phi + f_{\phi, \text{Re}_p} \right) \frac{(1 - \phi) (\mathbf{u}_f[\mathbf{X}_p^{(i)}] - \mathbf{U}_p^{(i)})}{\tau_p}, \quad (16)$$

where

$$f_\phi = \frac{5.81\phi}{(1-\phi)^2} + 0.48 \frac{\phi^{1/3}}{(1-\phi)^3}, \quad (17a)$$

$$f_{\phi, \text{Re}_p} = \phi^3(1-\phi) \text{Re}_p \left( 0.95 + \frac{0.61\phi^3}{(1-\phi)^2} \right). \quad (17b)$$

The fluctuating drag force is updated in time according to Eq. (6). However, special care needs to be taken when integrating stochastic differential equations, as classical schemes for deterministic ordinary differentials are not strongly consistent for stochastic differentials [49]. The integration of Eq. (6) is handled via an explicit RK scheme that exhibits first-order strong and weak convergence (see Chap. 11 of [49]),

$$F''_{d,k}{}^{n+1} = (1-a^n)F''_{d,k}{}^n \Delta t + b^n \Delta W_t + \frac{\Delta W_t^2 - \Delta t}{2\sqrt{\Delta t}} [b^{n+1/2} - b^n], \quad (18)$$

where  $F''_{d,k}{}^n$  is the  $k$ th component of the fluctuating force at the  $n$ th time iteration,  $a = 1/\tau_F$ ,  $b = \sqrt{2}\sigma_F/\sqrt{\tau_F}$ , and  $\Delta W_t = \sqrt{\Delta t} \mathcal{N}[0, 1]$ . As shown in Sec. III, the coefficients of the OU process in Eq. (6) are only a function of hydrodynamic variables. Therefore,  $b^{n+1/2}$  is evaluated at the midpoint step resulting from second-order RK integration of the particle position and velocity. The third term on the right-hand side of Eq. (18) corresponds to a finite difference approximation for spatial variation in  $b$ , while the other two terms comprise the standard Euler-Maruyama method. Therefore, Eq. (18) will simplify to the Euler integration scheme for homogeneous OU coefficients. Initialization of the fluctuating force is achieved by sampling from the steady Fokker-Planck solution  $\mathcal{N}[0, \sigma_F]$ . Since a soft-sphere collision model is employed here, the time step  $\Delta t$  required to accurately resolve collisions guarantees the OU stability criterion  $\Delta t \leq \tau_F$ .

## B. Fluid-phase description

In order to account for two-way coupling between the fluid and particle phases, without resolving the boundary layers around each particle, we consider a volume-filtered description for the fluid phase. Specifically, the pointwise Navier-Stokes equations are replaced with locally smoothed conservation equations for mass and momentum [31],

$$\frac{\partial}{\partial t} [(1-\phi)\rho_f] + \nabla \cdot [(1-\phi)\rho_f \mathbf{u}_f] = 0, \quad (19a)$$

$$\frac{\partial}{\partial t} [(1-\phi)\rho_f \mathbf{u}_f] + \nabla \cdot [(1-\phi)\rho_f \mathbf{u}_f \otimes \mathbf{u}_f] = \nabla \cdot \boldsymbol{\tau} + (1-\phi)\rho_f \mathbf{g} - \mathcal{F}_{\text{inter}} + \mathcal{F}_{\text{mfr}}, \quad (19b)$$

where  $\mathbf{g}$  is the gravitational body force and  $\mathcal{F}_{\text{mfr}}$  is a forcing term utilized to establish a desired mass flow rate. The fluid stress tensor  $\boldsymbol{\tau}$  is given by

$$\boldsymbol{\tau} = -p_f \mathbf{I} + \mu_f \left[ \nabla \mathbf{u}_f + \nabla \mathbf{u}_f^T - \frac{2}{3} (\nabla \cdot \mathbf{u}_f) \mathbf{I} \right], \quad (20)$$

where  $p_f$  is the pressure and  $\mathbf{I}$  is the identity matrix. The source term due to interphase momentum transfer  $\mathcal{F}_{\text{inter}}$  is obtained by projecting each particle's hydrodynamic force onto the fluid mesh and is discussed in detail in Sec. IV C.

The fluid-phase conservation equations are solved using NGA [50], a fully conservative, low-Mach number finite volume solver. A staggered grid with second-order spatial accuracy is advanced in time with the semi-implicit Crank-Nicolson scheme of Pierce [51], while the pressure Poisson equation is solved via fast Fourier transforms to enforce continuity. We emphasize that the particle and fluid equations are staggered in time such that the particle equations are solved using the fluid velocity obtained from an Adams-Bashforth predictor step, which is second-order accurate, resulting in second-order temporal accuracy for the coupling between particles and fluid phase.

### C. Two-way coupling

The projection of particle data onto the Eulerian grid is performed by way of a Gaussian kernel  $\mathcal{G}(\|\mathbf{x} - \mathbf{X}_p^{(i)}\|)$ ,

$$\phi = \sum_{i=1}^{N_p} \mathcal{G}(\|\mathbf{x} - \mathbf{X}_p^{(i)}\|) \mathcal{V}_p^{(i)}, \quad (21a)$$

$$\mathcal{F}_{\text{inter}} = \sum_{i=1}^{N_p} \mathcal{G}(\|\mathbf{x} - \mathbf{X}_p^{(i)}\|) \mathbf{F}_{\text{inter}}^{(i)}, \quad (21b)$$

with characteristic size  $\delta_f$  that corresponds to the full width at half height. Unless otherwise stated, the Gaussian kernel in this work was held fixed at  $\delta_f = 7d_p$ . The operations given in Eqs. (21a) and (21b) are computed efficiently by a two-step filtering procedure, where the particle data are first extrapolated to the nearest grid points on the fluid mesh and then diffused implicitly to the characteristic width of the kernel  $\delta_f$  [4], thereby yielding Eulerian fields that are spatially smooth.

### D. Granular temperature computation

While the standard deviation in drag force in Eq. (13a) is straightforward to compute with the resolved fields in an EL simulation, the mean-free time in Eq. (8) is more challenging due to its implicit dependence on the granular temperature,  $\Theta$ . Since the physical mechanism for force-velocity decorrelation is attributed to collisions, the random uncorrelated particle motion must be utilized in Eq. (8) [44]. Special care needs to be taken when evaluating the mean particle velocity about which the fluctuation is defined. Capecelatro *et al.* [52] showed that in flows with significant heterogeneity in volume fraction (i.e., clustered flows), defining the mean particle velocity using the same procedure employed for two-way coupling results in a strong dependence on the choice of filter size  $\delta_f$ . Instead, an accurate representation of the spatially correlated velocity can be obtained using an adaptive filter that dynamically adjusts its sampling volume such that a sufficient number of particles are evaluated at each spatial location. The adaptive filter is given by [52]

$$\delta_{\Theta}(\phi) = \left( \frac{\mathcal{N}_p d_p^3}{\phi} \right)^{1/3}, \quad (22)$$

to compute the granular temperature over  $\mathcal{N}_p = 10$  nearest neighbors. For clarity, we note that  $\delta_f$  denotes a fixed Gaussian filter width employed for two-way coupling of momentum, but  $\delta_{\Theta}$  denotes a variable Gaussian filter width for computing the granular temperature. Projecting particle data with the variable Gaussian filter  $\mathcal{G}_{\Theta}$  leads to

$$\phi_{\Theta} = \sum_{i=1}^{N_p} \mathcal{G}_{\Theta}(\|\mathbf{x} - \mathbf{X}_p^{(i)}\|) \mathcal{V}_p^{(i)}, \quad (23a)$$

$$\phi_{\Theta} \mathcal{U}_p = \sum_{i=1}^{N_p} \mathcal{G}_{\Theta}(\|\mathbf{x} - \mathbf{X}_p^{(i)}\|) \mathcal{V}_p^{(i)} \mathbf{U}_p^{(i)}. \quad (23b)$$

Defining the particle velocity fluctuation  $\delta \mathbf{U}_p^{(i)}$  with respect to the local phasic average,

$$\delta \mathbf{U}_p^{(i)} = \mathbf{U}_p^{(i)} - \frac{\phi_{\Theta} \mathcal{U}_p[\mathbf{X}_p^{(i)}]}{\phi_{\Theta}[\mathbf{X}_p^{(i)}]}, \quad (24)$$

allows the granular temperature at the particle to be computed as

$$\Theta[\mathbf{X}_p^{(i)}] = \frac{1}{3} \delta \mathbf{U}_p^{(i)} \cdot \delta \mathbf{U}_p^{(i)}. \quad (25)$$

TABLE I. Simulation conditions.

$d_p$	$500 \times 10^{-6}$ m
$\mu_f$	$1.0 \times 10^{-5}$ Pa s
$\rho_f$	$1.0$ kg/m <sup>3</sup>
$\langle \phi \rangle$	[0.1 0.4]
$\text{Re}_m$	[10 100]
$\rho_p/\rho_f$	[100 1000]

In summary, the adaptive filtering utilized to obtain Eq. (25) has been previously shown to accurately replicate two-point Lagrangian statistics (radial distribution function and velocity autocorrelation) [52] and allows for the computation of uncorrelated particle motion within inhomogeneous flows, since it relies upon a local average of the particle velocity. For homogeneous flows, the granular temperature is equivalent to the particle velocity variance  $T$ ; see additional discussion in Sec. V. The same two-step filtering process in Sec. IV C is employed for Eqs. (23a) and (23b), with the key difference being that the diffusion coefficient is now a spatially varying quantity [see Eq. (22)].

## V. HOMOGENEOUS FLUIDIZATION OF ELASTIC PARTICLES

We consider the homogeneous fluidization of particles within a triply periodic cube of length  $L$ . A mean fluid flow rate  $\langle \mathbf{u}_f \rangle = [0 \ 0 \ u_{f,z}]^\top$  is imposed via  $\mathcal{F}_{\text{mfr}}$  in Eq. (19b) to obtain a desired mean Reynolds number  $\text{Re}_m$ , while the gravitational body force  $\mathbf{g} = [0 \ 0 \ -g_z]^\top$  is prescribed in the opposite direction.  $\mathcal{F}_{\text{mfr}}$  is added as a uniform source term and is computed each time step to enforce the constant  $u_{f,z}$ . The body force  $g_z$  is set equal to the mean hydrodynamic acceleration  $\langle \mathbf{F}_d \rangle / m_p$ , computed via Eq. (16) for the mean conditions  $\text{Re}_m$  and  $\langle \phi \rangle$ . For the homogeneous cases considered here, the drag force offsets the weight of the suspension, leading to a mean particle velocity that is approximately zero throughout the simulation. In contrast, the particle velocity variance will grow or decay to a steady value that is dictated by the balance of drag variation and hydrodynamic dissipation. The simulation domain closely reflects the PR-DNS studies of Tenneti *et al.* [8] and Tavanashad *et al.* [29], which serve as benchmark data for comparison to the stochastic EL method presented here. Unless otherwise noted, the grid spacing  $\Delta x/d_p = 0.5$ , kernel width  $\delta_f/d_p = 7$ , and domain size  $L/d_p = 7$  were held fixed for the homogeneous fluidization simulations, and a summary of relevant conditions is provided in Table I.

Within the homogeneous fluidization system, we define two canonical flows that result from different initial conditions for the particle velocity. Namely, we first examine the fluidized homogeneous heating system (FHHS) in Sec. V B, where particles are initialized with zero velocity and particle velocity variance grows to a steady value. We then examine the fluidized homogeneous cooling system (FHCS) in Sec. V C, where particles are initialized with an overprescribed velocity variance that decays to a steady value. To match the FHCS simulations completed by Tenneti *et al.* [8], we sample the initial particle velocities from a Maxwellian distribution.

It is important to note that the domain sizes  $L$  considered by the PR-DNS studies of Tenneti *et al.* [8] and Tavanashad *et al.* [29] are sufficiently small that particle clustering is not observed and the system remains homogeneous. It has been well established that large-scale fluidized systems exhibit the classic clustering instability due to two-way momentum coupling and/or dissipative collisions. We first focus on the homogeneous case and define crucial parameters to facilitate comparison between EL and PR-DNS benchmark data. Specifically, particle velocity variance  $T$  is computed with a velocity fluctuation,

$$\mathbf{U}_p^{(i)'} = \mathbf{U}_p^{(i)} - \langle \mathbf{U}_p^{(i)} \rangle, \quad (26)$$

which is defined with respect to the domain average  $\langle U_p^{(i)} \rangle$ , leading to

$$T = \frac{1}{3} \langle U_p^{(i)'} \cdot U_p^{(i)'} \rangle. \quad (27)$$

Utilizing the definition for particle velocity fluctuation in Eq. (26) and particle velocity variance in Eq. (27), we define the particle Reynolds stress tensor  $\mathbf{R}^p$ , anisotropy tensor  $\mathbf{b}^p$ , and thermal Reynolds number  $\text{Re}_T$  as

$$\mathbf{R}^p = \langle U_p' \otimes U_p' \rangle, \quad (28a)$$

$$\mathbf{b}^p = \frac{\mathbf{R}^p}{3T} - \frac{1}{3} \mathbf{I}, \quad (28b)$$

and

$$\text{Re}_T = \frac{\rho_f d_p \sqrt{T}}{\mu_f}. \quad (29)$$

We emphasize that the mean-free time  $\tau_{\text{col}}$  in Eq. (8) is always computed with the granular temperature  $\Theta$  via Eq. (25), making it valid for inhomogeneous flows. However, when comparing to PR-DNS of homogeneous systems, we report Eqs. (28a)–(29) with the particle velocity variance  $T$ , computed via Eq. (27), for consistency with the definitions employed in those studies. In Sec. VI, we finally consider large-scale simulations of cluster-induced turbulence (CIT) that are characterized by strong inhomogeneities in particle number density and clusters that fall faster than their terminal velocity.

### A. Convergence

Before drawing detailed comparisons between the stochastic EL framework presented here, standard EL framework, and PR-DNS, the convergence properties of EL with  $\delta_f$  variation are examined within the FHHS. As discussed in Sec. IV C,  $\delta_f$  sets the filter length scale for two-way coupling and is therefore directly related to variation in the fluid fields through the projection of  $\mathcal{V}_p^{(i)}$  and  $\mathbf{F}_{\text{inter}}^{(i)}$ . Variation in  $\phi$  and  $\mathbf{u}_f$  will lead to variation in the quasisteady drag contribution  $\mathbf{F}_d^{(i)*}$ , thereby providing a mechanism for the generation of particle velocity variance.

We note that the FHHS has been examined in detail via PR-DNS with freely evolving particles by Tang *et al.* [53] and Tenneti *et al.* [8]. In these works, it was shown that the FHHS is characterized by a rapid growth and sustainment of particle velocity variance. Additionally, Tang *et al.* [53] reported isotropic particle velocity fluctuations. Here, the anisotropy tensor  $\mathbf{b}^p$  and thermal Reynolds number  $\text{Re}_T$  are examined at fixed simulation conditions  $\text{Re}_m = 20$ ;  $\langle \phi \rangle = 0.1$ ;  $\rho_p/\rho_f = 100$  and varying filter size  $\delta_f/d_p = 1, 2, 4, 7, 16$  (see Fig. 4). The stochastic EL framework presented here yields  $\text{Re}_T$  curves that are consistent with PR-DNS observations, and a steady state velocity variance that is relatively insensitive to  $\delta_f$  refinement. While the trace of the particle Reynolds stress tensor is not a strong function of  $\delta_f$  with stochastic EL, the anisotropy is directly linked to the projection width. Specifically, stochastic EL yields isotropic velocity fluctuations for larger filter widths,  $\delta_f/d_p \geq 4$ , but converges to the same anisotropy as standard EL as the filter width is refined. By contrast, with standard EL, the particle velocity variance *and* anisotropy are a direct function of  $\delta_f$ . As the filter width is increased in standard EL, the ensuing particle velocity fluctuations become more anisotropic and biased to the streamwise direction. For sufficiently small filter widths,  $\delta_f/d_p \leq 2$ , the particle velocity variance predicted by standard EL approaches that predicted by stochastic EL, which is consistent with the resolution criteria obtained by Liu *et al.* [54] for the Gaussian envelope in force coupling methods. However, it is emphasized that standard EL never yields the rapid  $T$  growth observed with stochastic EL, and the variation in  $\mathbf{F}_d^{(i)*}$  does not converge to the PR-DNS value (see Table II). Thus, discrepancies between standard EL and PR-DNS cannot be completely removed by refining the filter width since standard EL *infers* drag statistics from resolved

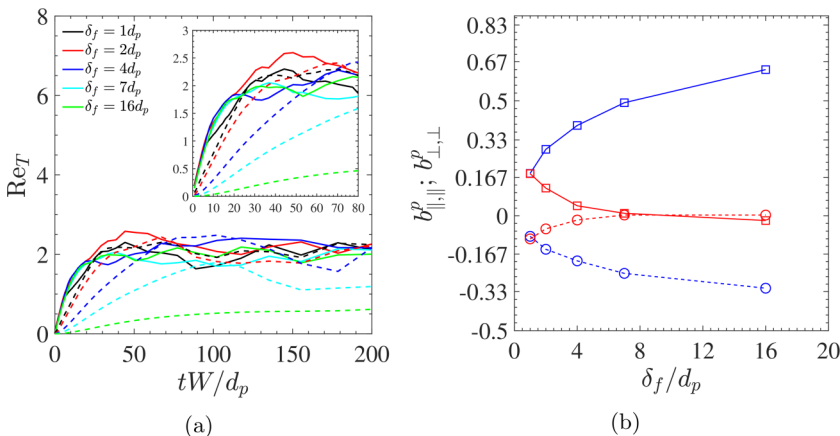


FIG. 4. (a)  $Re_T$  evolution in the FHHS at  $Re_m = 20$ ;  $\langle\phi\rangle = 0.1$ ;  $\rho_p/\rho_f = 100$  with varying  $\delta_f$ ; solid lines denote stochastic EL and dashed lines denote standard EL. (b) Mean of the anisotropy tensor at steady state in the streamwise  $b_{\parallel,\parallel}^p$  (square) and transverse  $b_{\perp,\perp}^p$  (circle) directions; red denotes stochastic EL, while blue denotes standard EL.

hydrodynamic fields that are not exact, whereas the stochastic EL framework *specifies* drag force statistics through  $\mathbf{F}_d^{(i)''}$ . Finally, we note that first- and third-order interpolation schemes were tested, with no appreciable change being observed.

As prefaced at the end of Sec. II, EL employs locally interpolated fluid quantities and instantaneous particle velocities to evaluate the hydrodynamic force acting on a particle. Consequently, force variance may be introduced into an EL simulation through the resolved fields. In fact, the dependence of velocity variance on filter width with the standard EL framework is a direct consequence of increased variation in resolved fields with decreasing  $\delta_f$ . To quantify the degree of force variation introduced by  $\mathcal{V}_p^{(i)} \nabla \cdot \boldsymbol{\tau}$  and  $\mathbf{F}_d^{(i)*}$ , we compute the variance in these terms (denoted as  $\sigma_{un}^2$  and  $\sigma_{qs}^2$ , respectively) at the steady state and normalize them by the force variance obtained from Eq. (13a) at the mean conditions reported in Table II,  $\sigma_F^2(Re_m, \langle\phi\rangle)$ . For  $\delta_f/d_p \leq 2$ , standard EL yields variation in the quasisteady drag that is comparable to PR-DNS, but does not converge to  $\sigma_F^2(Re_m, \langle\phi\rangle)$ . For the largest filter width ( $\delta_f/d_p = 16$ ), standard EL smears hydrodynamic fields to such a degree that negligible variance in quasisteady drag occurs. Since stochastic drag generates velocity variance independent of the resolved fields,  $\sigma_{qs}^2$  will not tend to zero as  $\delta_f \rightarrow \infty$  with the stochastic EL framework. Specifically, the particle velocity variance will feed back into the particle Reynolds number and  $\sigma_{qs}^2$  will tend to a constant as  $\delta_f \rightarrow \infty$  with the stochastic EL framework. At sufficiently small filter widths,  $\delta_f/d_p \leq 2$ , stochastic EL leads to overpredictions for  $\sigma_{qs}^2$  since

TABLE II. Resolved force variances.

$\delta_f/d_p$	Standard EL		Stochastic EL	
	$\sigma_{un}^2/\sigma_F^2(Re_m, \langle\phi\rangle)$	$\sigma_{qs}^2/\sigma_F^2(Re_m, \langle\phi\rangle)$	$\sigma_{un}^2/\sigma_F^2(Re_m, \langle\phi\rangle)$	$\sigma_{qs}^2/\sigma_F^2(Re_m, \langle\phi\rangle)$
16	$4.1 \times 10^{-5}$	0.002	$9.5 \times 10^{-6}$	0.163
7	$2.3 \times 10^{-4}$	0.127	$5.5 \times 10^{-5}$	0.210
4	$1.3 \times 10^{-3}$	0.589	$3.9 \times 10^{-4}$	0.400
2	$6.7 \times 10^{-3}$	0.944	$6.2 \times 10^{-4}$	1.432
1	$5.8 \times 10^{-2}$	1.380	$5.4 \times 10^{-2}$	2.000

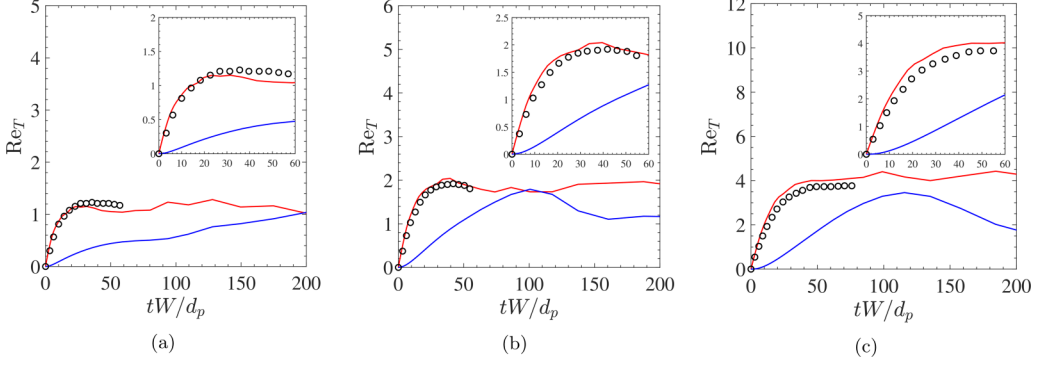


FIG. 5. FHHS at (a)  $Re_m = 10$ , (b)  $Re_m = 20$ , and (c)  $Re_m = 50$ . Stochastic EL (red lines), standard EL (blue lines), and PR-DNS results (black circles). All cases were simulated at  $\langle \phi \rangle = 0.1$ ;  $\rho_p/\rho_f = 100$ .

standard EL already yields force variation that is comparable to  $\sigma_F^2(Re_m, \langle \phi \rangle)$ . Future work that examines predictor-corrector methods for obtaining an exact force variance for arbitrary filter width would be useful. However, we do not consider such a task here but note that the resolved force variances at  $\delta_f/d_p = 7$  are of secondary significance in the homogeneous fluidization simulations.

### B. Fluidized homogeneous heating system (FHHS)

In addition to the qualitative trends presented in Sec. V A, we draw direct comparison between PR-DNS, stochastic EL, and standard EL for the evolution of particle velocity variance in the FHHS.  $Re_T$  curves presented in Tenneti *et al.* [8] at varying  $Re_m$  and fixed ( $\langle \phi \rangle$ ;  $\rho_p/\rho_f$ ) are employed as benchmark data for the comparisons illustrated in Fig. 5. For the  $Re_m$  range considered in Fig. 5, the stochastic EL framework is in strong agreement with the PR-DNS results and captures not only the steady value of velocity variance, but also the temporal growth. On the other hand, standard EL underpredicts the steady velocity variance and the temporal growth. Considering varying  $\langle \phi \rangle$  and fixed ( $Re_m$ ;  $\rho_p/\rho_f$ ), a comparison is drawn in Fig. 6 to the PR-DNS data of Tavanashad *et al.* [29]. Similar trends are observed at varying solids volume fraction, where stochastic EL is in strong agreement with PR-DNS but the standard EL fails to build sufficient particle velocity variance. The error bars in Fig. 6 correspond to 95% confidence intervals computed over five realizations from

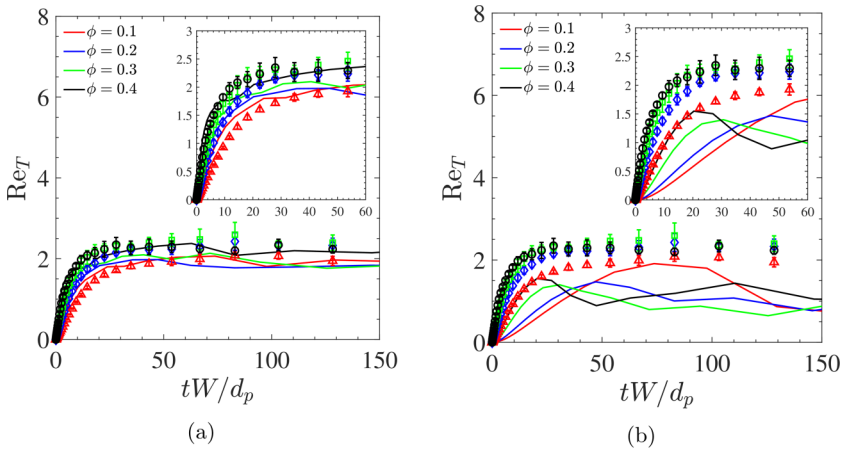


FIG. 6. FHHS with (a) stochastic FL and (b) standard EL at  $\langle \phi \rangle = 0.1, 0.2, 0.3, 0.4$ ;  $Re_m = 20$ ;  $\rho_p/\rho_f = 100$ . PR-DNS data (markers) and EL simulations (solid lines).

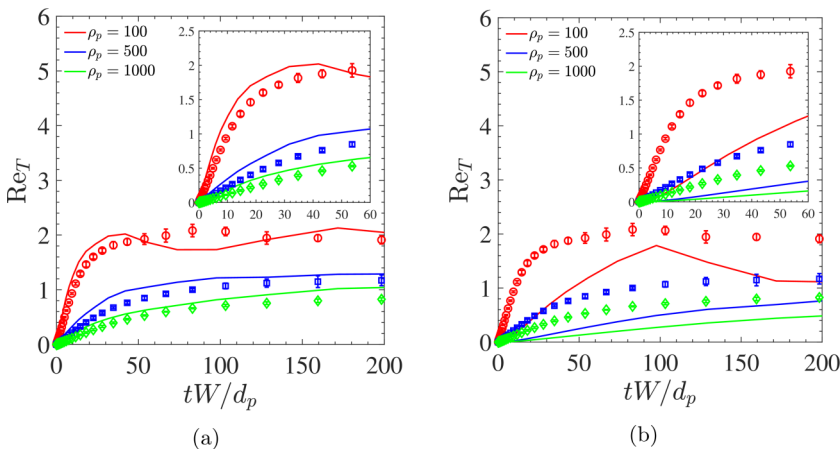


FIG. 7. FHHS with (a) stochastic FL and (b) standard EL at  $\rho_p/\rho_f = 100, 500, 1000$ ;  $\text{Re}_m = 20$ ;  $\langle\phi\rangle = 0.1$ . PR-DNS data (markers) and EL simulations (solid lines).

the data of Tavanashad *et al.* [29]. We note that error bars are only provided here when comparing to the data of Tavanashad *et al.* [29]. Finally, we compare stochastic EL and standard EL to the PR-DNS data of Tavanashad *et al.* [29] at varying  $\rho_p/\rho_f$  and fixed ( $\text{Re}_m$ ;  $\langle\phi\rangle$ ) in Fig. 7. Combining the results obtained in Figs. 5–7, it becomes apparent that standard EL neglects the role of subgrid, neighbor-induced, drag fluctuations and, consequently, cannot capture the variance and dispersion obtained in homogeneous simulations. These results are consistent with the data provided in Tenneti *et al.* [39], where quasisteady drag was shown to act as a sink to granular temperature, causing standard EL frameworks to be overly dissipative in homogeneous fluidization.

### C. Fluidized homogeneous cooling system (FHCS)

For the FHHS system considered in Sec. VB, the suspension dynamics are dominated by fluid-mediated sources to particle velocity variance, since particles are initialized with zero velocity. By contrast, the FHCS system is initialized with an overprescribed velocity variance and is thus dominated by hydrodynamic sinks to velocity variance. Directly extracting the fluid-mediated sources and sinks from PR-DNS shows that the FHHS and FHCS stress these two terms, respectively (see Fig. 8 of [8]). As a result, the agreement between standard EL and PR-DNS is expected to improve for the FHCS since standard EL captures dissipation due to quasisteady drag but not sources due to neighbor effects. Considering the  $\text{Re}_T$  curves from Tenneti *et al.* [8] as benchmark data, a comparison is drawn in Fig. 8 between PR-DNS, stochastic EL, and standard EL for the FHCS at fixed ( $\text{Re}_m$ ;  $\langle\phi\rangle$ ;  $\rho_p/\rho_f$ ) and varying  $\text{Re}_{T,0}$  initial condition. In the FHCS, standard EL captures the temporal decay of velocity variance quite well, but fails to sustain the correct velocity variance at the steady state. By contrast, stochastic EL captures the temporal decay and steady velocity variance when compared to PR-DNS. These results highlight that the error observed with a standard EL method can depend upon the dynamics of the system, i.e., heating vs cooling, in addition to the hydrodynamic regime considered.

### D. Role of anisotropy

It was shown in previous sections that the force Langevin model leads to improved predictions for  $T(t)$  with less-resolved hydrodynamic fields ( $\delta_f/d_p = 7$ ). However, the isotropic formulation given by Eq. (6) will not replicate force anisotropy or anisotropy in the particle Reynolds stresses, which may be present in real systems. To probe the effect of such phenomena, we first consider force probability distribution functions (PDFs) extracted from FHHS at the steady state and compare with

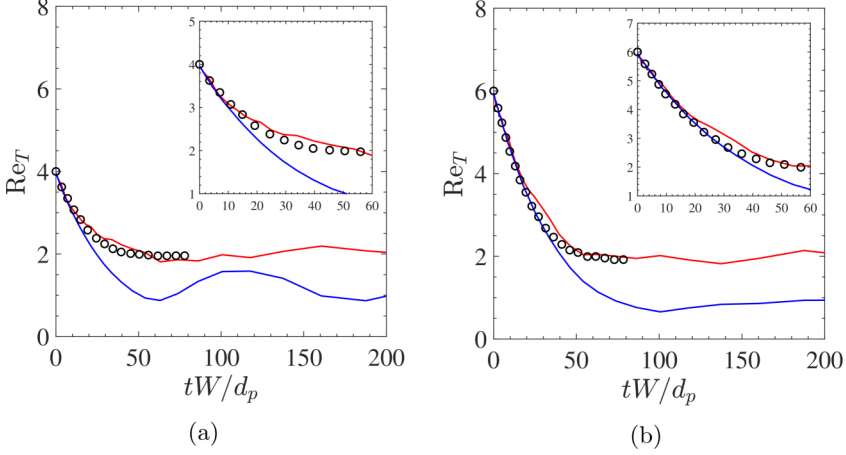


FIG. 8. FHCS initialized with (a)  $\text{Re}_{T,0} = 4$  and (b)  $\text{Re}_{T,0} = 6$ . Stochastic EL (red lines), standard EL (blue lines), and PR-DNS results (black circles). All cases were simulated at  $\text{Re}_m = 20$ ;  $\langle \phi \rangle = 0.1$ ;  $\rho_p/\rho_f = 100$ .

data extracted from PR-DNS (see Fig. 9). For the direction parallel to the mean flow,  $F''_{d,\parallel}$  is normally distributed with a standard deviation that matches PR-DNS and the correlation in Eq. (13a). For the transverse direction,  $F''_{d,\perp}$  again recovers the specified normal distribution, but the standard deviation is overpredicted by  $\sim 2\times$  when compared to the PR-DNS data. Therefore, the present model would benefit from appropriate parametrization of the standard deviation in transverse hydrodynamic force. Furthermore, examining  $\mathbf{R}^p$  predicted by PR-DNS shows that the off-diagonal components are two orders of magnitude less than the smallest diagonal. For that reason, we focus on  $b''_{\parallel,\parallel}$ ;  $b''_{\perp,\perp}$  predicted by PR-DNS (see Fig. 10). Finite anisotropy is observed in the particle Reynolds stresses that is most pronounced at lower Reynolds numbers and lower solids volume fractions. It is interesting to note that the magnitude of  $b''_{\parallel,\parallel}$ ;  $b''_{\perp,\perp}$  illustrates  $R''_{\parallel,\parallel}/R''_{\perp,\perp} \in [1.0, 2.4]$ , which is consistent with the force anisotropy observed in Fig. 9. Thus, future work would benefit from numerically probing the implications of  $\sigma_{F,\parallel} \neq \sigma_{F,\perp}$  in the force Langevin model, as well as analytical examination of the collisional redistribution of particle Reynolds stresses.

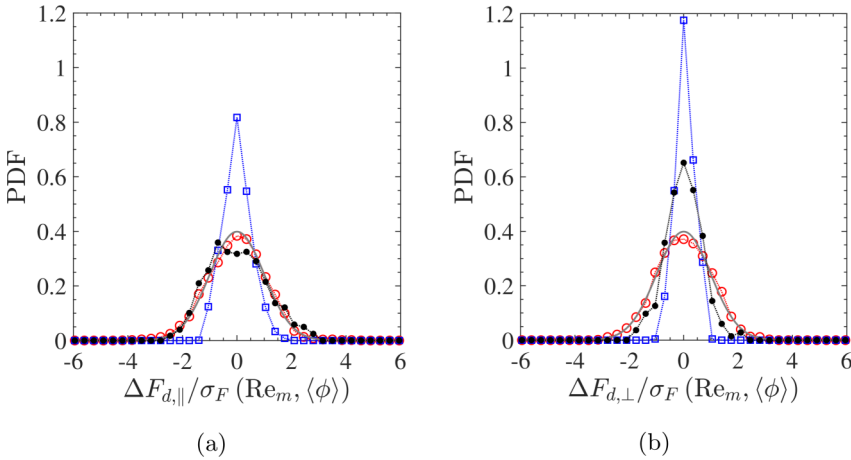


FIG. 9. Probability distributions in the FHCS for (a) streamwise and (b) transverse hydrodynamic forces.  $\circ$ : fluctuating drag  $\mathbf{F}''_d$ ;  $\square$ : quasisteady drag  $\mathbf{F}^*_d$ ;  $\bullet$ : PR-DNS results; and  $—$ :  $\mathcal{N}[0, \sigma_F(\text{Re}_m, \langle \phi \rangle)]$ . Removal of the mean from the PDF is denoted as  $\Delta F_d$ . Conditions are given by  $\text{Re}_m = 20$ ;  $\langle \phi \rangle = 0.1$ ;  $\rho_p/\rho_f = 100$ .

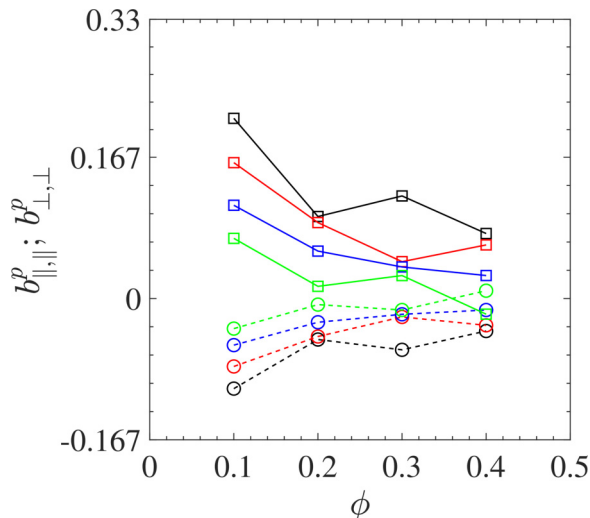


FIG. 10. Anisotropy in the particle Reynolds stress tensor as predicted by PR-DNS. Square markers correspond to the streamwise  $b_{||,||}^p$  and circles correspond to the transverse  $b_{\perp,\perp}^p$ .  $Re_m$  values of 10 (black), 20 (red), 50 (blue), and 100 (green) are considered.

## VI. CLUSTER-INDUCED TURBULENCE (CIT)

Until this point, the domain size of the systems under consideration was small enough such that instabilities giving rise to heterogeneity in particle concentration were suppressed. However, large-scale flows with inertial particles will lead to the spontaneous formation of clusters due to two-way momentum coupling and/or dissipative collisions [52,55,56] (see Fig. 11). As discussed by Fullmer and Hrenya [56], neighbor-induced drag fluctuations act as a source of granular temperature that may contribute to cluster break up. To probe the role of neighbor effects on cluster statistics, we consider simulations of fully developed cluster-induced turbulence (CIT) with standard EL and stochastic EL. The CIT simulation geometry is essentially identical to the homogeneous fluidization described in Sec. V, with the exception that the domain length is increased to resolve the cluster length scale [55],

$$\mathcal{L} = \tau_p^2 g_z. \quad (30)$$

Following Capecelatro *et al.* [57], we set the streamwise domain length as  $L_x = 32\mathcal{L}$  to obtain converged statistics and avoid clusters falling in their own wakes. The simulation conditions are summarized in Table III. To quantify the degree of particle segregation in homogeneous isotropic turbulence, Eaton and Fessler [58] proposed a clustering parameter  $D$ ,

$$D = \frac{\langle (\phi - \langle \phi \rangle)^2 \rangle^{1/2} - \sigma_p}{\langle \phi \rangle}, \quad (31)$$

TABLE III. Simulation conditions.

$d_p$	$90 \times 10^{-6}$ m	$\Delta x/d_p$	3
$\mu_f$	$1.0 \times 10^{-5}$ Pa s	$\delta_f/d_p$	7
$\rho_f$	$1.0$ kg/m <sup>3</sup>	$\mathcal{L}/d_p$	100
$\langle \phi \rangle$	0.05	$L_x/\mathcal{L}$	8
$Re_m$	1	$L_y/\mathcal{L}$	8
$\rho_p/\rho_f$	1000	$L_z/\mathcal{L}$	32

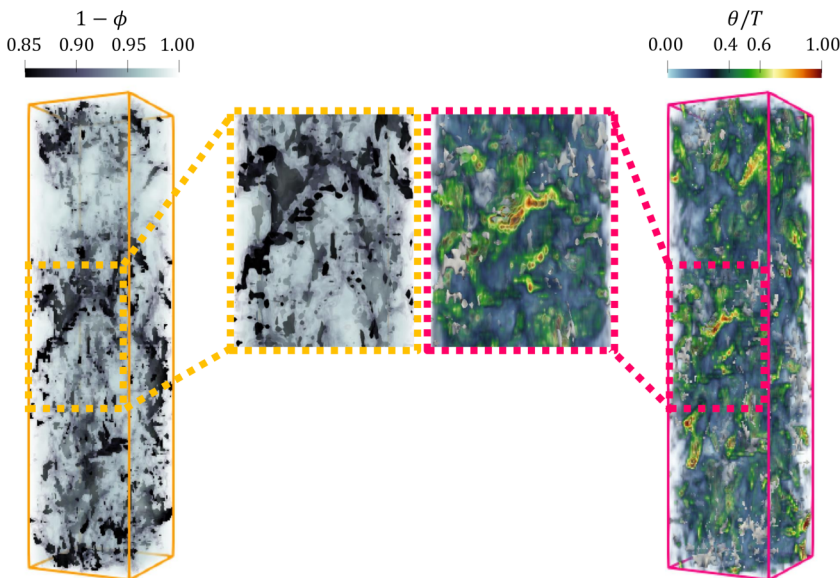


FIG. 11. Cluster formation in CIT illustrated by volume rendering of the instantaneous fluid volume fraction (left) and normalized granular temperature (right). Insets demonstrate that granular temperature is largely generated at the interface of clusters where large inhomogeneities exist, which is consistent with previous results obtained by Capecelatro *et al.* [52].

where  $\sigma_p$  is the standard deviation in the solids volume fraction for a random distribution of particles (evaluated at the beginning of the simulation for the initial random particle configuration). Here, we utilize  $D$  as an indicator of the degree of clustering within the entire domain, so as to probe the effect of neighbor-induced drag fluctuations on cluster break up. While  $D$  provides an estimate for the degree of clustering, we note that more detailed descriptions of heterogeneous media have been proposed that depend upon the viewing window size [59,60]. While these methods are beyond the scope of the present work, they do provide a more inclusive picture of the clustering spectrum, as opposed to a single value obtained with  $D$ .

Due to the presence of clusters, CIT exhibits drag reduction when compared to homogeneous systems. Specifically, entrainment of the surrounding fluid by particle clusters leads to a mean particle velocity in the streamwise direction  $\langle U_{p,z} \rangle$  that is nonzero and in the direction of gravity [see Fig. 12(a)]. We note that simulations are completed here in a reference frame that moves with the mean slip velocity  $W_z$ , which is specified by the mean Reynolds number  $Re_m$  and the assumption that  $\langle U_{p,z} \rangle \approx 0$ ; see discussion in Sec. V. Therefore, drag reduction in CIT leads to particle acceleration in the direction of gravity and mean settling velocities in the present simulations that are  $\sim 2.25W_z$ . Examining the evolution of mean particle settling velocity over the course of the simulations shows there are negligible differences between stochastic EL and standard EL [see Fig. 12(a)]. Similarly, negligible differences are observed between stochastic EL and standard EL for the clustering parameter [see Fig. 12(c)]. Since the degree of clustering is tied to drag reduction, and by extension the mean settling velocity,  $D$  and  $\langle U_{p,z} \rangle$  are strongly correlated. For example, a significant reduction in  $D$  would be reflected in an increase in  $\langle U_{p,z} \rangle$ , due to drag enhancement from homogenization of the particle phase. Since  $D$  and  $\langle U_{p,z} \rangle$  show consistent behavior, i.e., no appreciable change with the stochastic EL method, the model for neighbor-induced drag does not play a significant role in these domain averaged quantities, though it may alter the spectra obtained from the method of Quintanilla and Torquato [60].

Similar to mean settling velocity and clustering parameter, the particle velocity variance also shows minor deviation between stochastic and standard EL during transients and at the steady

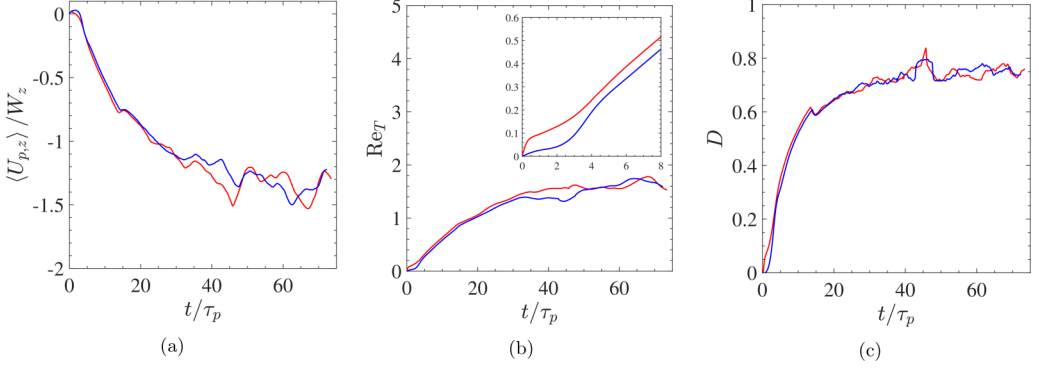


FIG. 12. Evolution of the (a) normalized mean particle velocity, (b) particle velocity variance, and (c) clustering parameter in CIT. Blue is standard EL and red is stochastic EL.

state; see Fig. 12(b). However, the beginning of the simulation  $t/\tau_p \in [0, 5]$  does show significant deviation between the velocity variance developed with stochastic EL and standard EL [see inset of Fig. 12(b)]. At this point, particles are randomly, but still homogeneously, distributed within the domain. Under these conditions, the neighbor-induced drag fluctuation is the predominate source of velocity variance since clusters with sharp solids volume fraction interfaces have yet to form. As the system enters the transient stage  $t/\tau_p \in [5, 30]$ , mesoscale particle structuring begins and the solids accelerate in the streamwise direction. The formation of clusters leads to significant quasisteady drag variance at the edge of clusters, where large gradients in solids volume fraction and fluid velocity occur. These quasisteady drag variances are resolved by a standard EL method and will facilitate granular temperature transport through the cluster via shear generation and collisional conduction; see right panel of Fig. 11. Therefore, heterogeneous systems provide additional sources to particle velocity variance that can dominate over the neighbor effect. As further evidence, we extract probability distributions for quasisteady and fluctuating drag in CIT (see Fig. 13). For the case of homogeneous fluidization in Fig. 9, fluctuating drag is more significant than quasisteady drag, while in the case of CIT, the exact opposite holds. Furthermore, the streamwise component of quasisteady drag tends to a log-normal distribution in CIT, while the transverse component

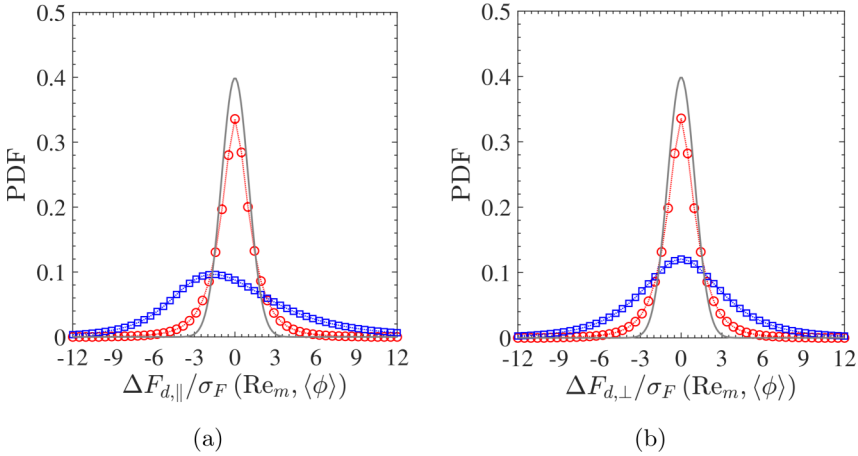


FIG. 13. Probability distributions in CIT for (a) streamwise and (b) transverse hydrodynamic forces.  $\circ$ : fluctuating drag  $F_d''$ ;  $\square$ : quasisteady drag  $F_d^*$ ; and  $—$ :  $\mathcal{N}[0, \sigma_F^2(\text{Re}_m, \langle \phi \rangle)]$ . Removal of the mean from the PDF is denoted as  $\Delta F_d$ .

remains relatively Gaussian. In addition, we reiterate that the stochastic force is isotropic and was shown, in Sec. V A, to yield isotropic particle velocity fluctuations in homogeneous fluidization. However, for the case of CIT, stochastic EL and standard EL yield the same anisotropy,  $b_{\parallel,\parallel}^p = 0.35$  and  $b_{\perp,\perp}^p = -0.16$ , which is further evidence that resolved quasisteady drag is dominant over neighbor-induced drag.

## VII. CONCLUSIONS

In the present study, we examine the role of higher-order drag statistics, originating from neighbor-induced fluid flow perturbations, in Eulerian-Lagrangian (EL) methods. A model was proposed for neighbor-induced hydrodynamic forces by treating the fluctuating drag as a stochastic variable that follows an Ornstein-Uhlenbeck process. Specifically, the force Langevin (FL) method detailed in Lattanzi *et al.* [19] was utilized here to construct a stochastic EL framework. Closures are provided for the theoretical inputs to the FL equation, integral timescale  $\tau_F$ , and force standard deviation  $\sigma_F$ , which are appropriate for inertial particles at moderate Reynolds numbers. Specifically, the integral timescale of the fluctuating drag is approximated with the mean-free time between successive collisions, derived from the kinetic theory of nonuniform gases. The standard deviation in drag force is closed with a different correlation based upon particle-resolved direct numerical simulation (PR-DNS) of fixed assemblies. The stochastic EL framework specifies unresolved drag statistics through the stochastic force, leading to the correct evolution and sustainment of particle velocity variance when compared to PR-DNS of freely evolving homogeneous suspensions. Since standard EL infers drag statistics from variations in the resolved flow, it cannot replicate the higher-order particle statistics (velocity variance and dispersion) observed in PR-DNS of homogeneous suspensions. Finally, the role of neighbor-induced drag fluctuations on cluster-induced turbulence (CIT) is considered. In contrast to homogeneous fluidization, CIT is characterized by large gradients in solids volume fraction and fluid velocity. The aforementioned gradients provide a source for drag variance in standard EL, through the quasisteady drag closure, that can dominate over neighbor effects. Since standard EL resolves the dominant modes for generating granular temperature in heterogeneous systems—quasisteady drag variation at cluster interface and collisional conduction—we observe negligible change when employing the stochastic EL framework.

While emphasis is placed here on inertial particle suspensions at moderate solids loading and Reynolds numbers, we stress that the proposed methodology is a general framework that may be adapted to a variety of applications. Namely, the concept of higher-order drag statistics can be readily applied to higher-order statistics in Nusselt and Sherwood correlations, employed for the simulation of heat and/or mass transfer. Additionally, compressible particle-laden flows often exhibit significant drag variation *and* unsteady effects (added mass and Basset history). The present framework provides a stepping stone that may be leveraged by future work to account for such effects.

## ACKNOWLEDGMENTS

This material is based upon work supported by the National Science Foundation under Grants No. CBET-1904742 and No. CBET-1438143. The authors acknowledge the Texas Advanced Computing Center (TACC) for providing Stampede2 compute resources under Extreme Science and Engineering Discovery Environment (XSEDE) Grant No. TG-CTS200008.

The authors report no conflict of interest.

---

[1] P. Cundall and O. Strack, A discrete numerical model for granular assemblies, *Géotechnique* **29**, 47 (1979).

- [2] Y. Tsuji, T. Kawaguchi, and T. Tanaka, Discrete particle simulation of two-dimensional fluidized bed, *Powder Technol.* **77**, 79 (1993).
- [3] M. van der Hoef, M. van Sint Annaland, N. Deen, and J. Kuipers, Numerical simulation of dense gas-solid fluidized beds: A multiscale modeling strategy, *Annu. Rev. Fluid Mech.* **40**, 47 (2008).
- [4] J. Capecelatro and O. Desjardins, An Euler–Lagrange strategy for simulating particle-laden flows, *J. Comput. Phys.* **238**, 1 (2013).
- [5] M. Mehrabadi, S. Tenneti, R. Garg, and S. Subramaniam, Pseudo-turbulent gas-phase velocity fluctuations in homogeneous gas–solid flow: Fixed particle assemblies and freely evolving suspensions, *J. Fluid Mech.* **770**, 210 (2015).
- [6] G. Shallcross, R. Fox, and J. Capecelatro, A volume-filtered description of compressible particle-laden flows, *Intl. J. Multiphase Flow* **122**, 103138 (2020).
- [7] S. H. L. Kriebitzsch, M. A. van der Hoef, and J. A. M. Kuipers, Fully resolved simulation of a gas-fluidized bed: A critical test of DEM models, *Chem. Eng. Sci.* **91**, 1 (2013).
- [8] S. Tenneti, M. Mehrabadi, and S. Subramaniam, Stochastic Lagrangian model for hydrodynamic acceleration of inertial particles in gas–solid suspensions, *J. Fluid Mech.* **788**, 695 (2016).
- [9] G. Akiki, W. Moore, and S. Balachandar, Pairwise-interaction extended point-particle model for particle-laden flows, *J. Comput. Phys.* **351**, 329 (2017).
- [10] G. Akiki, T. L. Jackson, and S. Balachandar, Force variation within arrays of monodisperse spherical particles, *Phys. Rev. Fluids* **1**, 044202 (2016).
- [11] A. Esteghamatian, M. Bernard, M. Lance, A. Hammouti, and A. Wachs, Micro/meso simulation of a fluidized bed in a homogeneous bubbling regime, *Intl. J. Multiphase Flow* **92**, 93 (2017).
- [12] Z. Huang, H. Wang, Q. Zhou, and T. Li, Effects of granular temperature on inter-phase drag in gas-solid flows, *Powder Technol.* **321**, 435 (2017).
- [13] S. Subramaniam and S. Balachandar, Towards combined deterministic and statistical approaches to modeling dispersed multiphase flows, in *Droplets and Sprays : Applications for Combustion and Propulsion*, Energy, Environment, and Sustainability, edited by S. Basu, A. Agarwal, A. Mukhopadhyay, and C. Patel (Springer, Singapore, 2018), pp. 7–42.
- [14] A. Fortes, D. Joseph, and T. Lundgren, Nonlinear mechanics of fluidization of beds of spherical particles, *J. Fluid Mech.* **177**, 467 (1987).
- [15] G. Akiki, T. Jackson, and S. Balachandar, Pairwise interaction extended point-particle model for a random array of monodisperse spheres, *J. Fluid Mech.* **813**, 882 (2017).
- [16] A. Seyed-Ahmadi and A. Wachs, Microstructure-informed probability-driven point-particle model for hydrodynamic forces and torques in particle-laden flows, *J. Fluid Mech.* **900**, A21 (2020).
- [17] G. Akiki and S. Balachandar, Shear-induced lift force on spheres in a viscous linear shear flow at finite volume fractions, *Phys. Fluids* **32**, 113306 (2020).
- [18] A. Esteghamatian, F. Euzenat, A. Hammouti, M. Lance, and A. Wachs, A stochastic formulation for the drag force based on multiscale numerical simulation of fluidized beds, *Intl. J. Multiphase Flow* **99**, 363 (2018).
- [19] A. Lattanzi, V. Tavanashad, S. Subramaniam, and J. Capecelatro, Stochastic models for capturing dispersion in particle-laden flows, *J. Fluid Mech.* **903**, A7 (2020).
- [20] D. Haworth and S. Pope, A generalized Langevin model for turbulent flows, *Phys. Fluids* **29**, 387 (1986).
- [21] B. Sawford, Reynolds number effects in Lagrangian stochastic models of turbulent dispersion, *Phys. Fluids* **3**, 1577 (1991).
- [22] S. Pope, Lagrangian PDF methods for turbulent flows, *Annu. Rev. Fluid Mech.* **26**, 23 (1994).
- [23] S. Pope, A stochastic Lagrangian model for acceleration in turbulent flows, *Phys. Fluids* **14**, 2360 (2002).
- [24] I. Iliopoulos, Y. Mito, and T. Hanratty, A stochastic model for solid particle dispersion in a nonhomogeneous turbulent field, *Intl. J. Multiphase Flow* **29**, 375 (2003).
- [25] J. Pozorski and S. Apte, Filtered particle tracking in isotropic turbulence and stochastic modeling of subgrid-scale dispersion, *Intl. J. Multiphase Flow* **35**, 118 (2009).
- [26] M. Pai and S. Subramaniam, Two-way coupled stochastic model for dispersion of inertial particles in turbulence, *J. Fluid Mech.* **700**, 29 (2012).

- [27] M. Gorokhovski and R. Zamansky, Modeling the effects of small turbulent scales on the drag force for particles below and above the Kolmogorov scale, *Phys. Rev. Fluids* **3**, 034602 (2018).
- [28] S. Pope and Y. Chen, The velocity-dissipation probability density function model for turbulent flows, *Phys. Fluids* **2**, 1437 (1990).
- [29] V. Tavanashad, A. Passalacqua, R. Fox, and S. Subramaniam, Effect of density ratio on velocity fluctuations in dispersed multiphase flow from simulations of finite-size particles, *Acta Mech.* **230**, 469 (2019).
- [30] M. Maxey and J. Riley, Equation of motion for a small rigid sphere in a nonuniform flow, *Phys. Fluids* **26**, 883 (1983).
- [31] T. Anderson and R. Jackson, Fluid mechanical description of fluidized beds. equations of motion, *Ind. Eng. Chem. Fundam.* **6**, 527 (1967).
- [32] S. Ergun and A. Orning, Fluid flow through randomly packed columns and fluidized beds, *Ind. Eng. Chem.* **41**, 1179 (1949).
- [33] C. Wen and Y. Yu, Mechanics of fluidization, *Chem. Eng. Prog. Sympos. Ser.* **62**, 100 (1966).
- [34] D. Gidaspow, *Multiphase Flow and Fluidization: Continuum and Kinetic Theory Descriptions* (Academic Press, San Diego, 1994).
- [35] R. Hill, D. Koch, and A. Ladd, Moderate-Reynolds-number flows in ordered and random arrays of spheres, *J. Fluid Mech.* **448**, 243 (2001).
- [36] R. Beetstra, M. A. v. d. Hoef, and J. A. M. Kuipers, Drag force of intermediate Reynolds number flow past mono- and bidisperse arrays of spheres, *AIChE J.* **53**, 489 (2007).
- [37] S. Tenneti, R. Garg, and S. Subramaniam, Drag law for monodisperse gas–solid systems using particle-resolved direct numerical simulation of flow past fixed assemblies of spheres, *Intl. J. Multiphase Flow* **37**, 1072 (2011).
- [38] G. Rubinstein, J. Derksen, and S. Sundaresan, Lattice Boltzmann simulations of low-Reynolds-number flow past fluidized spheres: Effect of Stokes number on drag force, *J. Fluid Mech.* **788**, 576 (2016).
- [39] S. Tenneti, R. Garg, C. Hrenya, R. Fox, and S. Subramaniam, Direct numerical simulation of gas-solid suspensions at moderate Reynolds number: Quantifying the coupling between hydrodynamic forces and particle velocity fluctuations, *Powder Technol. Select. Papers 2009 NETL Multiphase Flow Workshop*, **203**, 57 (2010).
- [40] V. Garzó, S. Tenneti, S. Subramaniam, and C. Hrenya, Enskog kinetic theory for monodisperse gas-solid flows, *J. Fluid Mech.* **712**, 129 (2012).
- [41] D. Koch and A. Sangani, Particle pressure and marginal stability limits for a homogeneous monodisperse gas-fluidized bed: Kinetic theory and numerical simulations, *J. Fluid Mech.* **400**, 229 (1999).
- [42] S. Chapman, T. Cowling, and D. Burnett, *The Mathematical Theory of Non-uniform Gases: An Account of the Kinetic Theory of Viscosity, Thermal Conduction and Diffusion in Gases* (Cambridge University Press, Cambridge, 1970).
- [43] D. Ma and G. Ahmadi, A kinetic model for rapid granular flows of nearly elastic particles including interstitial fluid effects, *Powder Technol.* **56**, 191 (1988).
- [44] P. Février, O. Simonin, and K. Squires, Partitioning of particle velocities in gas–solid turbulent flows into a continuous field and a spatially uncorrelated random distribution: theoretical formalism and numerical study, *J. Fluid Mech.* **533**, 1 (2005).
- [45] J. Wylie, D. Koch, and A. Ladd, Rheology of suspensions with high particle inertia and moderate fluid inertia, *J. Fluid Mech.* **480**, 95 (2003).
- [46] A. Lattanzi, V. Tavanashad, S. Subramaniam, and J. Capecelatro, Fluid-mediated sources of granular temperature at finite Reynolds numbers, [arXiv:2108.01777](https://arxiv.org/abs/2108.01777).
- [47] V. Tavanashad, A. Passalacqua, and S. Subramaniam, Particle-resolved simulation of freely evolving particle suspensions: Flow physics and modeling, *Intl. J. Multiphase Flow* **135**, 103533 (2021).
- [48] R. Clift, J. Grace, and M. Weber, *Bubbles, Drops, and Particles* (Dover, New York, 2013).
- [49] P. Kloeden and E. Platen, *Numerical Solution of Stochastic Differential Equations*, corrected ed. (Springer, Berlin, 1992).
- [50] O. Desjardins, G. Blanquart, G. Balarac, and H. Pitsch, High order conservative finite difference scheme for variable density low Mach number turbulent flows, *J. Comput. Phys.* **227**, 7125 (2008).

- [51] C. Pierce, Progress-variable approach for large-eddy simulation of turbulent combustion, Ph.D. thesis, Stanford University, 2001.
- [52] J. Capecelatro, O. Desjardins, and R. Fox, On fluid–particle dynamics in fully developed cluster-induced turbulence, *J. Fluid Mech.* **780**, 578 (2015).
- [53] Y. Tang, F. Peters, and J. Kuipers, Direct numerical simulations of dynamic gas-solid suspensions, *AIChE J.* **62**, 1958 (2016).
- [54] D. Liu, E. Keaveny, M. Maxey, and G. Karniadakis, Force-coupling method for flows with ellipsoidal particles, *J. Comput. Phys.* **228**, 3559 (2009).
- [55] K. Agrawal, P. Loezos, M. Syamlal, and S. Sundaresan, The role of meso-scale structures in rapid gas–solid flows, *J. Fluid Mech.* **445**, 151 (2001).
- [56] W. Fullmer and C. Hrenya, The clustering instability in rapid granular and gas-solid flows, *Annu. Rev. Fluid Mech.* **49**, 485 (2017).
- [57] J. Capecelatro, O. Desjardins, and R. Fox, Effect of domain size on fluid–particle statistics in homogeneous, gravity-driven, cluster-induced turbulence, *J. Fluids Eng.* **138**, 041301 (2016).
- [58] J. Eaton and J. Fessler, Preferential concentration of particles by turbulence, *Intl. J. Multiphase Flow* **20**, 169 (1994).
- [59] B. Lu and S. Torquato, Local volume fraction fluctuations in heterogeneous media, *J. Chem. Phys.* **93**, 3452 (1990).
- [60] J. Quintanilla and S. Torquato, Local volume fraction fluctuations in random media, *J. Chem. Phys.* **106**, 2741 (1997).